Nanoscale terahertz STM imaging of a metal surface

Yang Luo,[1,*] Vedran Jelic,[1,†] Gong Chen,[2,3] Peter H. Nguyen,[1] Yu-Jui Ray Liu,[1] Jesus A. M. Calzada,[1] Daniel J. Mildenberger,[1] and Frank A. Hegmann[1,‡]

[1]*Department of Physics, University of Alberta, Edmonton, Alberta T6G 2E1, Canada*
[2]*School of Physics and Engineering, Zhengzhou University, Zhengzhou 450052, China*
[3]*Hefei National Laboratory for Physical Sciences at the Microscale and Synergetic Innovation Center of Quantum Information & Quantum Physics, University of Science and Technology of China, Hefei, Anhui 230026, China*

(Received 29 August 2020; revised 22 October 2020; accepted 22 October 2020; published 16 November 2020)

Terahertz scanning tunneling microscopy (THz-STM) has enabled studies of ultrafast dynamics in materials down to the atomic scale. However, despite recent advances, more work is needed to better understand and quantify the subpicosecond THz pulse-induced tunnel currents and corresponding THz-STM images of nanoscale features on surfaces. Here, we perform THz-STM on a metal surface and fully characterize the observed THz pulse-induced tunnel current and nanoscale imaging at atomic steps and defects using a Bardeen tunneling model in a three-dimensional (3D) tip geometry. We show that the measured steady-state STM current-voltage curves can be used in our model to accurately map the observed ultrafast THz-induced tunnel currents and calibrate the magnitude of the near-field peak transient THz voltage bias in the tunnel junction. Peak THz voltage bias transients greater than 10 V across the STM junction are achieved leading to field emission of subpicosecond tunnel currents with current densities exceeding 10^9 A/cm^2 in THz-STM imaging of a Cu(111) surface. Our results establish an important benchmark for future studies in THz-STM by quantifying the ultrafast THz-induced currents and bias voltages in the tunnel junction and providing a 3D tunneling model for understanding and accurately simulating THz-STM images of nanoscale features on metal surfaces.

DOI: 10.1103/PhysRevB.102.205417

I. INTRODUCTION

Exploring ultrafast phenomenon on the nanoscale is crucial for the continuing development of nanoscience and nanotechnology [1–18]. By combining ultrafast single-cycle terahertz (THz) pulses with scanning tunneling microscopy (STM), THz-STM has been developed to explore ultrafast phenomenon with simultaneous subpicosecond time resolution and subnanometer spatial resolution. In THz-STM, single-cycle, picosecond-duration THz pulses focused on the metal tip of an STM induce strong localized transient electric fields in the tunneling junction, generating an ultrafast modulation of the bias voltage [3,8–10,14,15,18]. The intrinsic nonlinearity of the tunnel current in the junction as a function of bias voltage ($I-V$ curve) results in a rectification of the THz-induced tunnel current that can be measured with lock-in detection, revealing energy-dependent electron tunneling processes at subpicosecond timescales [8]. The characterization of the THz-induced bias voltage and simulation of the resulting transient tunnel current are therefore critical for studying ultrafast nanoscale phenomena with THz-STM.

The steady-state (DC) STM I–V curve could in principle provide a direct map of the THz-induced tunnel current. However, in THz-STM, the THz-induced transient current, I_{THz}, can be many orders of magnitude larger than typical steady-state currents, I_{DC}, used in STM. Thus, in THz-STM experiments the THz-induced currents are obtained with either larger transient bias voltages [3,9] or significantly smaller tip-sample distances [8,10] compared to steady-state STM, making it almost impossible to directly compare the THz-induced tunnel current to the corresponding DC tunnel current at the same tip-sample distance over the same bias window. Furthermore, it is possible that the THz voltage transient at the junction induces a tunnel current that does not map directly onto the steady-state STM I–V curve. For example, THz-STM on a Si(111)-(7 × 7) surface showed that the THz-STM current-voltage characteristic is fundamentally different from steady-state STM due to THz pulse-induced band bending, ultrafast charging of the surface, and nonequilibrium tunneling dynamics [10]. This naturally raises the question of how well we can understand the THz-induced transient tunnel current observed in THz-STM based on steady-state tunneling measurements and models.

Previously, one-dimensional (1D) tunneling models typically used in steady-state STM have been used to simulate THz-induced currents in THz-STM [3,8–10,14]. The Simmons model, which assumes an energy-independent density of states (DOS) in both the tip and sample, can provide an approximate description of the THz-induced tunnel current versus peak electric field, $E_{THz,pk}$, of the incident THz pulse. This approach provides reasonable agreement with the measured $I_{THz} - E_{THz,pk}$ curves [3,9] as well as THz-pulse autocorrelation measurements that measure the THz-induced tunnel current as a function of terahertz pulse overlap time [3,14]. The Bardeen model, which includes an energy-dependent DOS, has been used to model THz-STM on silicon

*luo10@ualberta.ca
†Present address: Department of Physics and Astronomy, Michigan State University, East Lansing, Michigan 48824, USA.
‡hegmann@ualberta.ca

 ©2020 American Physical Society

surfaces [10] and single pentacene molecules [8]. Compared with semiconductors, metal surfaces have a relatively small variation in their local DOS with energy [19–21], and tip-induced band-bending effects can be ignored due to a high concentration of free carriers. This suggests that the metal tip to metal surface junction is well suited for applying tunneling models [20,21], making such a system valuable for extending applications of THz-STM and understanding the origin of the THz-induced tunnel current. However, there have been no previous reports of THz-STM imaging of metal surfaces. Furthermore, at high bias voltages the apparent barrier height of the tunnel junction can be greatly reduced [22], resulting in significant tunnel currents from other regions of the tip apex and a correspondingly larger effective tunneling area compared to the low-bias regime [23]. Therefore, the geometry of the tip apex needs to be considered in order to accurately quantify the tunnel current and interpret THz-STM imaging at high bias voltages [23].

In this work, we investigate THz pulse-induced tunnel currents and THz-STM imaging on a Cu(111) metal surface. By applying the Bardeen tunneling model to a 3D tip-apex geometry and constraining the fit parameters with steady-state STM measurements, we are able to accurately simulate the ultrafast THz-STM tunnel currents and also quantify the magnitude of the THz-induced peak bias voltage in the junction. THz-induced voltage transients greater than 10 V are generated that greatly reduce the apparent barrier height and produce transient tunnel currents in the field emission regime over subpicosecond timescales more than a million times larger than the DC STM tunnel current. The increased tunneling area at the tip apex leads to distinct features in THz-STM imaging across atomic steps that can be understood and quantified with the 3D tunneling model.

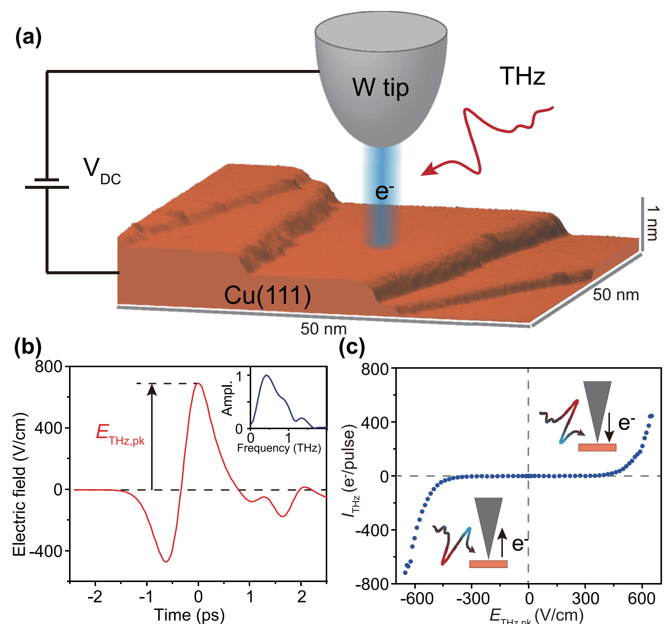

FIG. 1. (a) Schematic diagram of THz-STM on a Cu(111) surface. A THz pulse is coupled into the STM junction, inducing transient tunnel currents between the tungsten tip and the Cu(111) surface. (b) Incident THz-pulse electric-field waveform measured by free-space electro-optic sampling. Inset: Corresponding frequency spectrum. (c) THz-induced tunnel current, I_{THz}, as a function of the incident THz peak electric field, $E_{THz,pk}$, obtained with an open feedback loop (tip disengaged at $V_{DC} = 1$ V and $I_{DC} = 20$ pA, V_{DC} set to 0.1 V). Inset diagrams: Schematic of THz pulse polarity and corresponding rectified tunnel current direction of I_{THz}.

II. EXPERIMENTAL DETAILS

Our experiments were performed in an ultrahigh vacuum (UHV) STM system (RHK-UHV-SPM 3000) operating with a base pressure of $\sim 1 \times 10^{-10}$ Torr and an open-flow cryostat cooling the sample to ~100 K with liquid nitrogen. The Cu(111) surface was cleaned by cycles of argon ion sputtering and annealing. Electrochemically etched tungsten (W) tips used in all our experiments were cleaned by electron bombardment and field emission. The laser system consisted of a Ti:sapphire regenerative amplifier (Coherent RegA) seeded by a mode-locked oscillator (Coherent Micra), producing 4-μJ pulses with a center wavelength of 800 nm, a pulse duration of 80 fs, and a repetition rate of 250 kHz. An interdigitated photoconductive antenna (Laser Quantum Tera-SED10) was used for the generation of single-cycle THz pulses. The source was mounted on a motorized rotation stage for control of the THz pulse polarization and polarity at the junction, as well as the electric field strength. The waveform of the THz pulse was measured by electro-optic sampling in a 1-mm-thick (110)-cut ZnTe crystal. A polymethylpentene lens (Menlo Systems TPX lens) placed inside an inverted viewport fitted with a fused silica window to UHV was used to focus the THz beam onto the STM junction [10].

Figure 1(a) shows a schematic of the THz-STM experiments on an atomically flat Cu(111) surface, which has been widely studied with STM [24,25]. Single-cycle free-space propagating THz pulses [Fig. 1(b)] are focused onto the STM tip, leading to an ultrafast modulation of the bias voltage in the tunnel junction that generates a transient tunnel current. The incident THz-pulse train was modulated at 5077 Hz, well above the bandwidth of the STM feedback loop. The average THz-induced current, $I_{THz,avg}$ [A], was measured via lock-in detection. The rectified tunnel current induced by each THz pulse is given by $I_{THz}[e^-/\text{pulse}] = I_{THz,avg}/(e \times f_{rep})$, where f_{rep} $[Hz]$ is the repetition rate of the THz pulses and e is the electron charge. The minimum detectable I_{THz} was around 2 e^-/pulse, corresponding to an average current of 40 fA (with the modulation on) using a 10^9-V/A preamp (RHK IVP300). For THz-pulse autocorrelation measurements, the generated THz pulses were split with a high-resistivity silicon wafer to create a THz interferometer in which the optical path length of one arm was varied by moving a reflecting mirror mounted on a motorized linear stage [10].

In our experiment, the STM tip was positioned over a flat terrace with the DC bias voltage set to $V_{DC} = 1$ V and tunnel current setpoint at $I_{DC} = 20$ pA. Next, the STM feedback loop was switched off and V_{DC} was reduced to 0.1 V, which is negligible compared to the THz-induced bias voltages. The measured $I_{THz} - E_{THz,pk}$ curve is shown in Fig. 1(c), where the direction of the rectified current is consistent with the polarity of the THz pulses [10]. A rectified tunnel current of 450 e^-/pulse was obtained for an incident THz-pulse peak

field of 650 V/cm. This is equivalent to a peak current of $\sim$144 μA within a time window of about 0.5 ps, which is $\sim 7 \times 10^6$ times larger than the DC current setpoint of 20 pA. Such a high transient current suggests that the transient bias voltage is much larger than the DC bias setpoint of 1 V.

III. THEORETICAL MODEL

To estimate the enhanced electric field in the near-field of the tip and to understand the THz-induced tunnel current based on steady-state tunneling theories, we developed a model that accounts for both the steady-state STM and THz-STM measurements. For a 1D tunneling barrier, positive bias voltages drive electrons from the occupied DOS of the tip to the unoccupied DOS of the sample with a current density given by the Bardeen model with the image potential considered [20],

$$J(Z) = (4\pi e/\hbar)\int_0^{eV_b} d\varepsilon \rho_{\text{tip}}(\varepsilon - eV_b)\rho_{\text{sam}}(\varepsilon)T(\varepsilon, Z), \quad (1)$$

where V_b is the total bias voltage on the sample, which is the sum of the steady-state bias voltage, V_{DC}, and the ultrafast bias voltage induced by THz pulses, V_{THz}, such that $V_b = V_{\text{THz}} + V_{\text{DC}}$, $\rho_{\text{tip}}(\varepsilon)[\rho_{\text{sam}}(\varepsilon)]$ is the DOS for the tip (sample), and $T(\varepsilon, Z)$ is the transmission factor that depends on the energy of the electrons ε and the tip-sample separation Z. The potential barrier formed between two electrodes can be expressed as

$$\Phi(z) = eV_b + W_{\text{tip}} + (W_{\text{sam}} - W_{\text{tip}} - eV_b)\frac{z}{Z} + \Phi_{\text{im}}(z, Z), \quad 0 < z < Z, \quad (2)$$

where W_{tip} (W_{sam}) is the work function of the tip (sample),

$$\Phi_{im}(z, Z) = \frac{-e^2}{8\pi\epsilon_r\epsilon_0}\left[\frac{1}{2z} + \sum_{k=1}^{\infty}\left(\frac{kZ}{(kZ)^2 - z^2} - \frac{1}{kZ}\right)\right] \quad (3)$$

is the image potential induced by the two electrodes where ϵ_0 is the permittivity of free space and ϵ_r is the relative permittivity of the insulator [20,26]. The transmission factor is proportional to the probability that an electron with energy ε will penetrate the potential barrier, and is given within the Wentzel-Kramers-Brillouin approximation as

$$T(\varepsilon, Z) = \exp\left[-\frac{2}{\hbar}\int_{z_1}^{z_2} dz\sqrt{2m(\Phi(z, Z) - \varepsilon)}\right], \quad (4)$$

where z_1 and z_2 are the two roots of the equation $\Phi(z) - \varepsilon = 0$ $(z_1 < z_2)$. Due to the exponentially increasing transmission factor as a function of ε, the DOS close to the top of the bias window has a maximal contribution to the tunneling current.

The potential barrier is high when eV_b is much lower than the work functions, W, of the tip and sample [Fig. 2(a)], resulting in a high sensitivity of the tunnel current to changes in tip height. However, for $V_b > W/e$ [Fig. 2(b)], the shape of tunneling barrier is triangular rather than trapezoidal and the electrons tunnel though a greatly reduced effective barrier width compared to the actual gap size, namely, the STM operates in the field-emission regime [21,22]. This increases the effective tunneling area compared to the low-bias regime [23], such that tunnel currents from other regions of tip apex

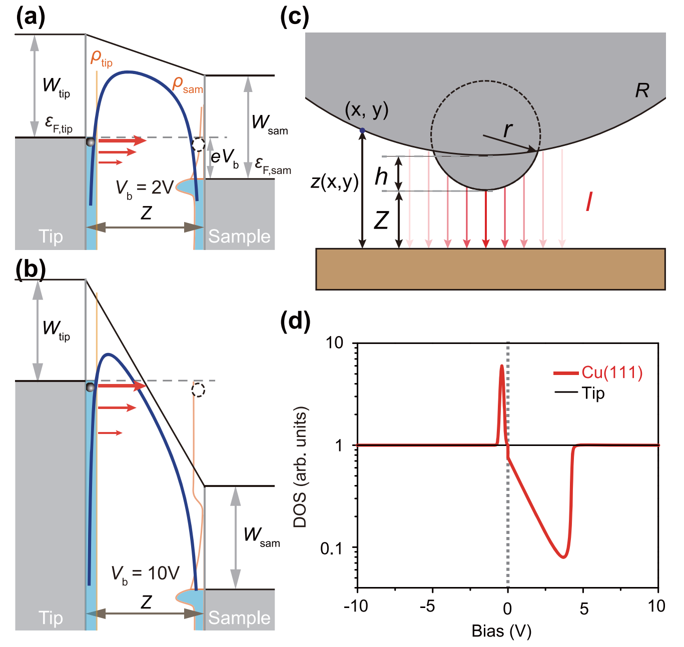

FIG. 2. Potential-energy landscape of the tunnel junction at (a) low- and (b) high positive bias voltages V_b, where W_{tip} (W_{sam}) is the work function of the tip (sample), $\varepsilon_{\text{F,tip}}$ ($\varepsilon_{\text{F,sam}}$) is the Fermi level of the tip (sample), and Z is the tip-sample distance. The DOS of the tip and sample are represented by ρ_{tip} and ρ_{sam}, respectively. The blue curve shows the potential barrier taking into account the image potential. There is enhanced tunneling from the occupied DOS of the tip into unoccupied DOS of the sample, where tunneling of electrons close to the Fermi level dominates. (c) Cross section of the 3D tunnel junction, where the STM tip is modeled by two spheres of radii r and R and relative offset h. The total tunnel current is obtained by integrating the current density over the surface of the tip apex. (d) DOS of tip and sample used in the simulation.

become significant. Thus, the geometry of the tip apex needs to be considered [23].

Typically, an STM tip has a radius of curvature of 50 nm or less at the tip apex. High-resolution imaging can often be achieved by controlled tip crashes resulting in an atomic cluster that is formed at the tip apex [20]. Therefore, to account for the 3D geometry of the tip-sample junction in our model, the tip apex is represented by a smaller sphere partially embedded within a larger sphere with radii of $r = 1$ nm and $R = 10$ nm, respectively, as shown in Fig. 2(c). The smaller sphere produces a small protrusion with a height, h, of 0.3 nm from the bottom of the larger sphere. The total tunnel current was calculated with a semiclassical approach by integrating the local current density over the tip surface, $I = \iint_{(x,y)} J(x, y, z(x, y))dxdy$, where x and y represent the spatial coordinates of the lower part of the tip surface. To simplify the model, we have assumed that the electrons tunnel vertically through the barrier. As our THz-STM measurements were conducted with a relatively small tip-sample distance of about 1 nm, the variations in the potential and field distribution around the emitter surface can be ignored [27,28]. The effect of tip geometry on the image potential is not considered here [29], and many-body effects are also ignored [30,31].

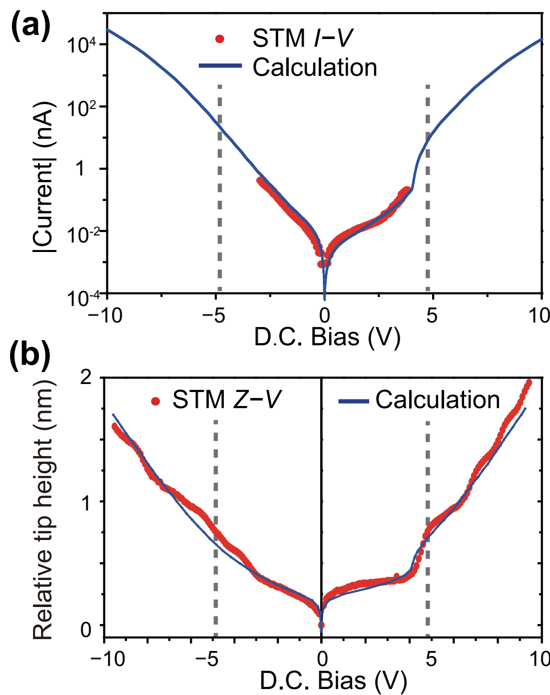

FIG. 3. (a) Experimental (red dots) and simulated (blue solid lines) steady-state STM *I–V* curve. The tunneling gap was set at 1 V and 20 pA. (b) Steady-state STM *Z–V* curves at a constant current of 20 pA. The gray dashed lines in (a) and (b) show the voltages corresponding to the work functions of the tip and sample.

The work function of a Cu(111) surface is around 4.94 eV [32]. The work function of tungsten is around 4.5–5.2 eV depending on the orientation of the crystal face. Here, we assumed the same work function for both the Cu(111) sample and the W tip, such that $W_{\mathrm{tip}} = W_{\mathrm{sub}} = 4.9$ eV. In most practical STM experiments, the DOS of the tip is assumed to be constant, such that $\rho_{\mathrm{tip}}(\varepsilon) = 1$. According to Bardeen's theory, the electrons tunnel from the occupied DOS of the tip into the unoccupied DOS of the sample at positive bias voltage. Following Ref. [22], the unoccupied DOS of Cu(111) is modeled based on the electronic band structure of the surface. At negative bias voltages, the electrons tunnel from the occupied DOS of the sample into the unoccupied DOS of the tip and the tunneling of electrons close to the Fermi level dominates. As the tunneling current is mainly from the surface electronic structure close to the Fermi energy [33], the occupied DOS of Cu(111) was determined by a Gaussian function centered at the peak energy of the surface state (−0.4 eV) and the variations of the DOS at high bias voltages were ignored, as shown in Fig. 2(d). In the field-emission regime, the electron emission is only dependent on the DOS of the emitter, which could be either the tip or the sample.

IV. RESULTS AND DISCUSSION

A. Single-point steady-state STM measurements

As shown in Fig. 3(a), the model closely matches the measured steady-state STM *I–V* curve in the bias window from −3 to +3.5 V. However, when the bias voltage exceeds the work function of the surface, the tunnel current increases rapidly and the junction becomes unstable, making it impossible to obtain constant-height $I_{\mathrm{DC}} - V_{\mathrm{DC}}$. curves over a wider range of bias voltages. Alternatively, an STM *Z–V* measurement, where the tip height can vary in order to maintain a constant tunnel current as the bias voltage is changed, allows access to higher bias voltages, albeit at larger tip-sample distances. As shown in Fig. 3(b), the good agreement between the experimental and calculated STM *Z–V* curves suggests that our model is able to accurately represent the tunneling process at both low- and high-voltage biases.

B. Single-point THz-STM measurements

Here, we show how our 3D tunnel junction model, with parameters set by the steady-state STM measurements, provides a universal fit to the measured ultrafast THz-STM response of the Cu(111) surface with subpicosecond THz-induced tunnel currents. The near-field THz waveform at the tip apex can be modified from that of the incident THz pulse due to the antenna properties of the tip [34,35]. Recent experiments have found that both the carrier-envelope phase and the spectral content of the THz near field in the STM junction can be modified by the geometric shape of the tip [14,15,18], although several THz-STM studies have used the electro-optically sampled THz waveform in their models [3,8–10]. In the theoretical model described here, the waveform of the transient bias voltage at the junction that provides an excellent fit to the observed THz-STM response is the same as the THz waveform obtained by electro-optic sampling [3,8–10]. The field enhancement factor, *F*, given as the ratio of the THz electric field in the near field of the junction to that of the incident THz pulse, $E_{\mathrm{THz,pk}}$, is inversely proportional to the tip-sample distance, while the THz-induced peak bias voltage, $V_{\mathrm{THz,pk}}$, stays constant for tip-sample distances less than 1 μm [10]. Thus, we assume a constant scaling factor, *S*, independent of tip-sample distance in order to determine the amplitude of THz-induced bias voltage from the incident THz-pulse electric field, such that $S[\mathrm{cm}] = V_{\mathrm{THz,pk}}[\mathrm{V}]/E_{\mathrm{THz,pk}}[\mathrm{V/cm}] = 1/45$ cm in all the model fits to the measurements.

The instantaneous value of the tunnel current at a given voltage was calculated following the steady-state *I–V* curve produced by our model (Fig. 3). As shown in Fig. 4(a), the calculated rectified current was obtained by the integral of the simulated tunnel current transient. Due to the highly nonlinear nature of the *I-V* curve, the dominant contribution to the rectified THz-induced tunnel current, I_{THz}, occurs at the peak of the THz-induced bias voltage. Figure 4(b) shows the experimental and simulated THz-STM $I_{\mathrm{THz}} - E_{\mathrm{THz,pk}}$ curves for both positive and negative polarities of the THz pulse, showing excellent agreement with our 3D model that is based on steady-state tunneling theory and the measured steady-state *I-V* curves. Current noise in our preamp and the 250-kHz repetition rate of the laser source limited the minimum detectable I_{THz} of our THz-STM system to about $2\,e^{-}$/pulse, which set the minimum $E_{\mathrm{THz,pk}}$ required to observe a THz-induced tunnel current to about +360 V/cm at positive-polarity THz electric fields and −315 V/cm at negative electric fields, corresponding to a $V_{\mathrm{THz,pk}}$ of about +8 and −7 V, respectively. A higher THz-induced current (or lower $E_{\mathrm{THz,pk}}$ onset) can be obtained at reduced tip-sample distances [8,10]; however,

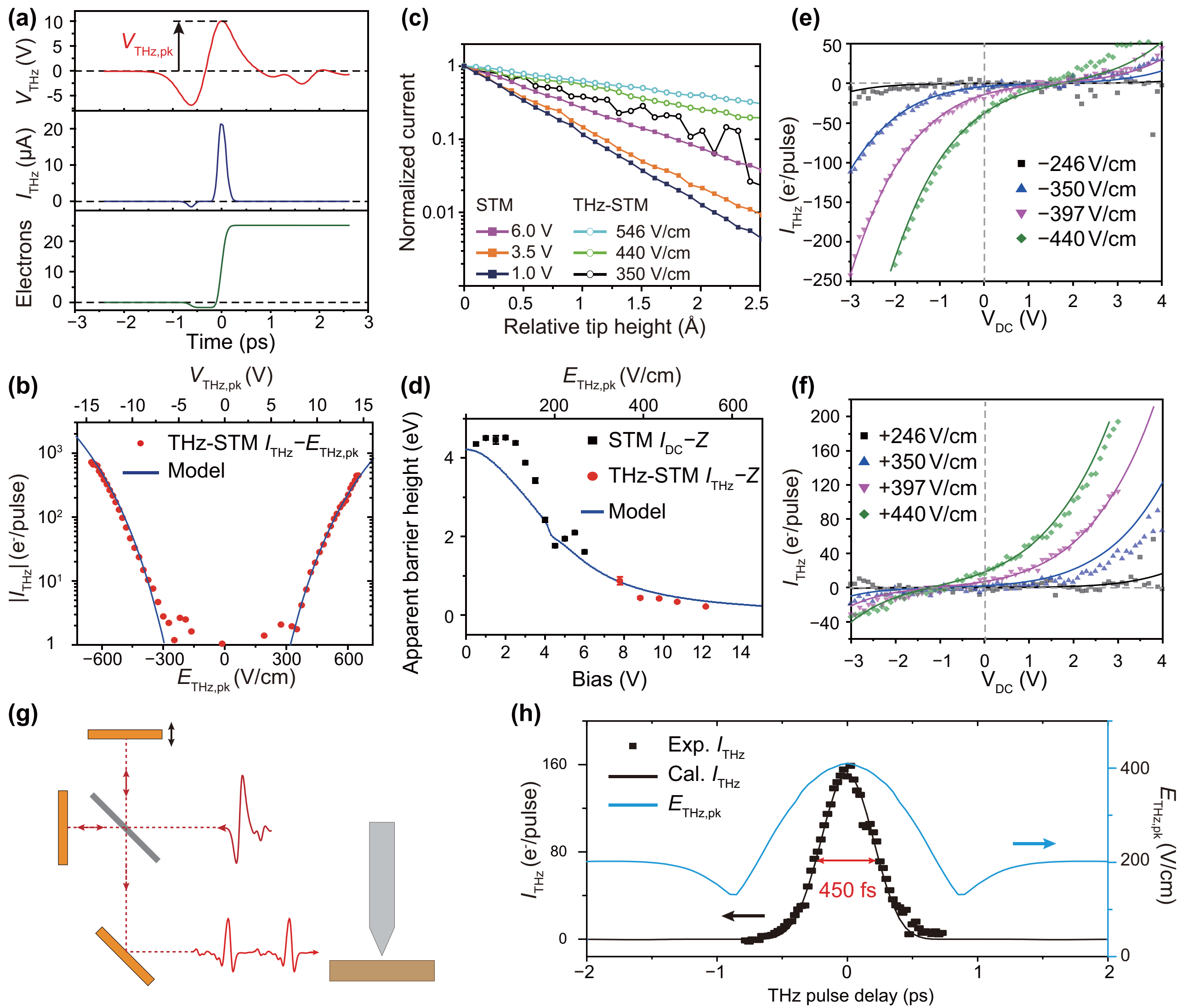

FIG. 4. (a) Simulated THz voltage transient (red solid line), ultrafast THz-induced current transient (blue solid line), and the integrated number of rectified electrons (green solid line) induced by the THz pulse based on the 3D tunneling model. (b) Experimental (red dots) and simulated (blue solid line) THz-STM $I_{\mathrm{THz}} - E_{\mathrm{THz,pk}}$ curves obtained with an open feedback loop ($V_{\mathrm{DC}} = 0.1$ V, tip disengaged at $V_{\mathrm{DC}} = 1$ V and $I_{\mathrm{DC}} = 20$ pA). (c) Experimental $I_{\mathrm{DC}} - Z$ and $I_{\mathrm{THz}} - Z$ curves as a function of relative tip height. STM I_{DC}–Z curves were obtained at initial currents of 50 pA. To obtain the $I_{\mathrm{THz}} - Z$ curves, the tip-sample separation was kept constant at the setpoint of $E_{\mathrm{THz,pk}} = 0$, $V_{\mathrm{DC}} = 0.1$ V, $I_{\mathrm{DC}} =$ 50 pA. (d) Experimental apparent barrier heights obtained from the $I_{\mathrm{THz}} - Z$ curves in (c) for steady-state STM (black dots) and THz-STM (red dots) and the calculated values (blue solid line). Experimental (dots) and simulated (solid lines) THz-induced current versus the DC bias voltage at (e) negative polarity and (f) positive polarity THz-pulse peak electric fields. In the measurements, the tip-sample separation was kept constant at the setpoint of $E_{\mathrm{THz,pk}} = 0$, $V_{\mathrm{DC}} = 2$ V, $I_{\mathrm{DC}} = 20$ pA. (g) Schematic of the THz-pulse autocorrelation measurement. (h) Experimental (black dots) and calculated (black solid line) I_{THz} as a function of autocorrelation overlap time for THz pulses ($V_{\mathrm{DC}} = 0.1$ V, $I = 40$ pA). The peak electric field of individual THz pulses is 205 V/cm. $E_{\mathrm{THz,pk}}$ of the combined THz pulses versus the autocorrelation overlap time (blue solid line) is also calculated. All fits use a near-field scaling factor of $S = 1/45$ cm and tip geometry parameters of $R = 10$ nm, $r = 1$ nm, and $h = 0.3$ nm.

increased local electric fields at smaller tip-sample distances can modify the surface through field-enhanced diffusion [36–38] or local sublimation induced by the tunneling electrons [39].

The tunnel barrier height is a fundamental parameter in STM. Experimentally, the exponential decay of an I–Z curve allows us to define an apparent barrier height (ABH) [10,20,21]. We have demonstrated that the THz-induced current in our system is detected in the field-emission regime since $V_{\mathrm{THz,pk}}$ is larger than the work function. Straightforward evidence for this phenomenon is an observed reduction in ABH for the THz-induced current, which was extracted from the exponential decay of the $I_{\mathrm{THz}} - Z$ curves, as shown in Fig. 4(c). In Fig. 4(d), the ABHs obtained from the STM $I_{\mathrm{DC}} - Z$ curves show a rapid decrease at bias voltages greater than 3 V, which is due to the rapid increase of the tunneling probability for applied bias potentials close to the work-function value. The $I_{\mathrm{THz}} - Z$ curves demonstrate even lower

ABHs, suggesting large peak-bias voltages that are in the field-emission regime.

Since the total bias, V_b, is the sum of the steady-state bias voltage and the ultrafast-bias voltage modulation induced by the enhanced THz-pulse electric field in the STM junction, we can demonstrate the accuracy of the field enhancement factor, F, by plotting I_{THz} versus V_{DC} for several incident THz peak fields. As shown in Figs. 4(e) and 4(f), The $I_{THz} - V_{DC}$ curves are well reproduced by our model using a scale factor of $S = 1/45$ cm, that is $V_{THz,pk} = 1$ V corresponds to $E_{THz,pk} = 45$ V/cm, equivalent to a field enhancement factor of $F \approx 2.2 \times 10^5$, similar to that reported previously [10]. As I_{THz} is primarily determined by the peak of the total bias, $V_{b,pk} = V_{DC} + V_{THz,pk}$, the scale factor, S, can also be estimated by fitting the $V_{DC} - E_{THz,pk}$ curves at constant I_{THz}, providing a calibration of the transient bias voltage in the junction.

The time resolution of THz-STM on the Cu(111) surface was determined by THz-pulse autocorrelation measurements described schematically in Fig. 4(g). As shown in Fig. 4(h), an autocorrelation width as small as 450 fs full width at half maximum is observed and accurately reproduced by the 3D tunneling model. Since the rectified THz-induced tunnel current is dominated by the peak of the transient bias voltage [Fig. 4(a)], such good agreement between experiment and theory suggests that the subcycle width of the THz-induced bias voltage in the junction is similar to that of the incident THz-pulse electric-field waveform obtained through electro-optic sampling.

C. Comparison to Fowler-Nordheim theory

Fowler-Nordheim (FN) theory can be used to estimate the current density due to field emission [40]. For an emitting object on the nanoscale, traditional FN theory needs to account for the image potential, as given by Refs. [41–44],

$$I_{EF} = \frac{e^3 A}{4hWt^2(y)}\left(\frac{V}{kR}\right)^2 \exp\left[-\frac{8\pi\sqrt{2mW^3}}{3he}\left(\frac{kR}{V}\right)v(y)\right], \quad (5)$$

where $y = \sqrt{e^3 V}/\sqrt{kRW^2}$, A is the emitting surface area, h is Planck's constant, W is the electron work function, R is the tip radius of the curvature of the tip, and k is a dimensionless factor that is determined by the local geometry of the tip. Lastly, $t(y)$ and $v(y)$ are two prefactors that can be found in Ref. [41]. A current-voltage characteristic following Eq. (5) would produce a straight line in a plot of $\ln(I/V^2)$ versus $1/V$. In the THz-STM experiments, we assume that I_{THz} is primarily from the peak of THz-induced bias voltage, $V_{THz,pk}$, and $V_{THz,pk}$ is proportional to $E_{THz,pk}$ by the scale factor of $S = 1/45$ cm. Plotting $\ln(I_{THz}/V_{THz,pk}{}^2)$ versus $1/V_{THz,pk}$ from the experimental $I_{THz} - E_{THz,pk}$ curve, as shown in Fig. 5, gives a straight line for the highest peak voltages ($V_{THz,pk} > 8$ V), consistent with field emission with $kR \approx 1$ nm. Theoretical studies that consider image interactions for nonsmooth emitters with small protrusions on the tip apex [27,45] suggest a value of $k \approx 0.1$, and thus $R \approx 10$ nm, which is consistent with our model of representing the tip by two spheres with radii of $R = 10$ nm and $r = 1$ nm.

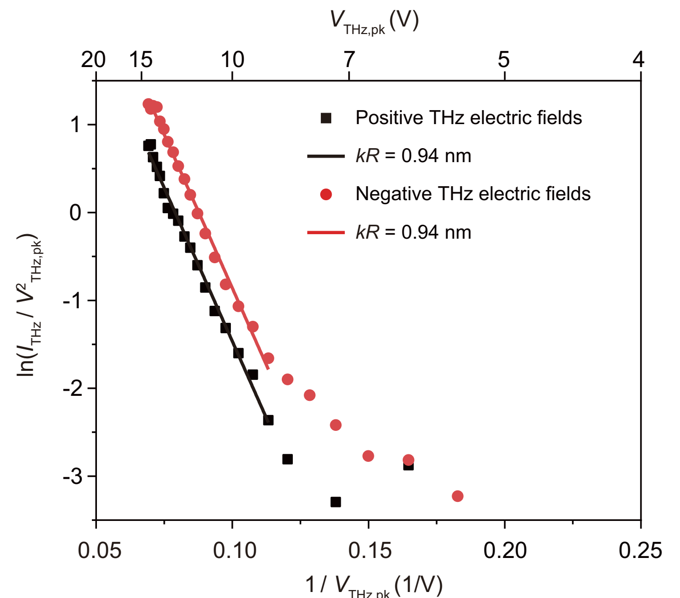

FIG. 5. Comparison of the measured THz-STM $I_{THz} - E_{THz,pk}$ curves (dots) to Fowler-Nordheim theory (solid lines) by plotting $\ln(I_{THz}/V_{THz,pk}{}^2)$ versus $1/V_{THz,pk}$, where $V_{THz,pk} = S \times E_{THz,pk}$.

D. THz-STM imaging of atomic steps on a metal surface

Atomic steps on metal surfaces are good imaging targets for THz-STM and an opportunity to expand the applicability of our model. Here, we first explore the differences between steady-state STM and ultrafast THz-STM by acquiring the THz-STM image with a small I_{THz} simultaneously with the constant-current steady-state STM image ($I_{THz} \ll I_{DC}$), as shown in Fig. 6(a) for a monoatomic step on the Cu(111) surface. An average THz-induced tunnel current of $I_{THz,avg} \sim 0.8$ pA was detected, which is much smaller than the DC current of ∼19.2 pA (feedback loop current setpoint is 20 pA). Thus, the feedback loop monitors the tunnel current mainly from I_{DC} and adjusts the tip height accordingly. However, the THz-STM image shows a different behavior near the step edge compared to STM. In order to understand the nanoscale features in the THz-STM image at the step edge, we simulated the spatial-dependent current density in a line profile across the atomic step edge using our 3D model, as shown in Fig. 6(b). The tip height was simulated across the step to maintain a constant current for a steady-state bias voltage of 1 V. As depicted schematically in Fig. 6(c), the THz-induced tunnel current at different tip positions along the line scan was then calculated by considering the peak THz-induced bias voltage of $V_{THz,pk} = 9.8$ V and a steady-state bias voltage of $V_{DC} = 1$ V. Since the effective tunneling area for THz-STM with a high transient bias voltage was larger than that for steady-state STM with a low DC bias voltage, the THz-induced tunnel current responded to the topographic structures on the surface over a larger area. As shown in Fig. 6(d), the current-density profiles, J_{THz}, evaluated at $V_{THz,pk}$ across the junction show significant differences at various tip positions along the step-edge line scan. The THz-induced current is reduced when the tip approaches the step edge from the upper part and

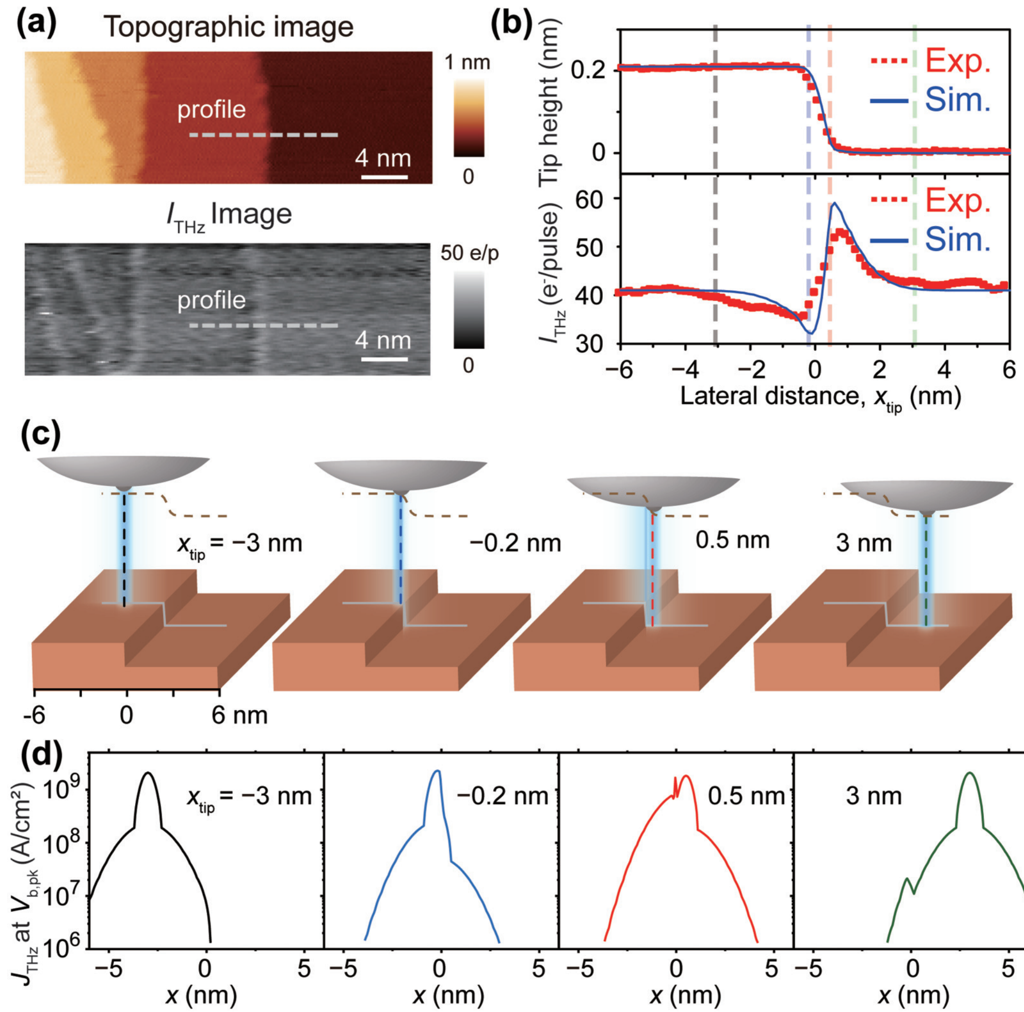

FIG. 6. (a) STM topography of the Cu(111) surface and the simultaneously acquired THz-STM image ($V_{DC} = 1$ V, $E_{THz,pk} = 440$ V/cm, $I_{DC} + I_{THz,avg} = 20$ pA, $I_{THz} \ll I_{DC}$). (b) Experimental (red dots) and simulated (blue solid lines) line scans for the relative tip height and the THz-induced tunnel current across a monatomic step along the dashed gray lines in (a). (c) Schematic of the tunneling junction at various lateral tip positions, x_{tip}, relative to the atomic step. The local magnitude of the THz-induced current density is illustrated by the relative transparency within the blue cylinder. (d) Calculated THz-induced current density at the peak bias voltage $V_{b,pk}$ at different x_{tip}.

increases when approaching from the lower part, which was well reproduced by our 3D model.

Our simulations suggest peak current densities exceeding 10^9 A/cm^2 with $I_{THz} \approx 40\ e^-$/pulse for THz-STM imaging [Fig. 6(d)] and up to 10^{10} A/cm^2 for single-point measurements [Fig. 4(b)]. To check this, if the measured $I_{THz,avg}$ autocorrelation width [Fig. 4(h)] and THz-STM spatial resolution [Figs. 6(a) and 6(b)] produce 40 electrons traversing the tunnel junction within 0.5 ps over an area of approximately 1 nm^2, then a peak transient current of about 13 μA and a current density of 1.3×10^9 A/cm^2 are produced, which is consistent with the peak current densities obtained in our 3D model calculations. THz pulse-induced current densities as high as 10^{11} A/cm^2 were observed in THz-STM imaging of Si(111) surfaces [10], making THz-STM a powerful tool for exploring extreme transient tunnel current densities in a variety of materials. We speculate that the higher bond strength between Si atoms on a Si(111) surface compared to that between Cu atoms on a Cu(111) allows for much higher THz pulse-induced tunnel current densities on a Si(111) surface before the onset of THz pulse-induced damage.

E. Terahertz-driven STM imaging of a metal surface

In terahertz-driven STM (TD-STM) imaging, $I_{THz,avg} \gg I_{DC}$ and the feedback loop adjusts the tip height according to $I_{THz,avg}$ [10]. STM and TD-STM imaging of atomic step edges and defects on the Cu(111) surface are shown in Figs. 7(a) and 7(b), respectively, with associated line scans in Figs. 7(c)–7(e). Although most of the single-atom defects on the terraces are not visible with TD-STM, some bigger defects were detected with reduced vertical resolution [Fig. 7(c)], which suggests that the THz-induced current is less sensitive to the change of tip-sample distance due to the high transient bias. The larger tunneling area in TD-STM gives a lateral resolution across a monatomic step edge of 2 nm compared to only 1 nm for steady-state STM [Fig. 7(d)]. However, the line profiles across a step edge with three atomic layers [Fig. 7(e)] are similar due to the larger change in tip height.

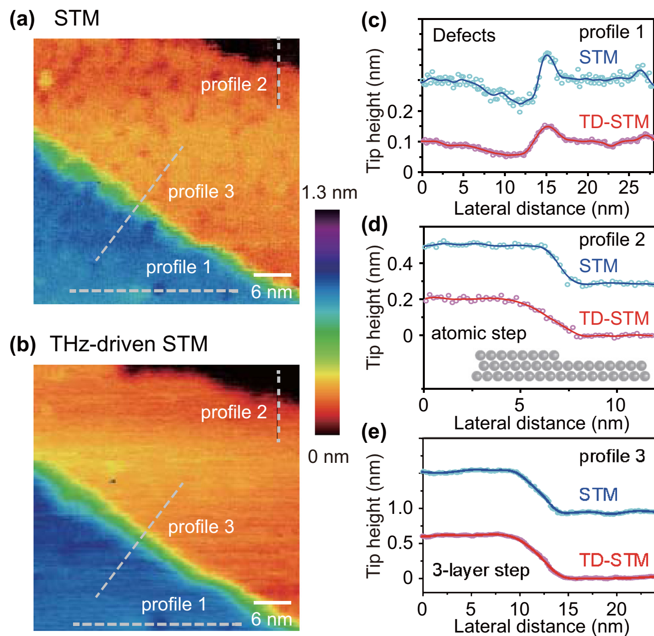

FIG. 7. (a) STM topography of the Cu(111) surface ($V_{DC} = 0.1$ V, $I_{DC} = 20$ pA)), showing atomic steps and defects. (b) THz-driven STM (TD-STM) of the same region as (a) with $E_{THz,pk} = 450$ V/cm, $I_{DC} + I_{THz,avg} = 20$ pA, $V_{DC} = 0.1$ V. Cross-sectional line scans for the relative tip height across (c) a defect, (d) a monatomic step, and (e) three-layer atomic step as identified by the profiles (gray dashed lines) in (a) and (b), showing the spatial resolution of STM and TD-STM.

While atomic resolution on semiconductor surfaces can be easily achieved with steady-state STM due to strongly localized dangling bonds and has been realized on Si(111) surface with TD-STM [10], resolving the atomic lattice of a close-packed metal surface requires a very short tip-sample separation [24,46,47]. The origin of the atomic resolution is understood by either the effect of a dangling bond at the tip apex or tip-sample interactions [20]. Due to the high DOS at the Fermi level of metal surfaces, a short tip-sample distance usually requires a large tunneling current, which reduces the stability of the tunneling junction. Thus, in our experiments the THz-STM signal was obtained by using high transient bias voltage instead of reducing the tip-sample distance. Atomic resolution and tip-sample interaction effects were not considered in our simulations.

The vertical and lateral resolutions at different bias voltages for a tip-sample distance of 1 nm can be determined following the methods proposed in Ref. [28]. As shown schematically in Figs. 2(a) and 2(b), as well as experimentally in Fig. 4(d), the tunnel barrier becomes smaller at higher bias voltages. This results in a decrease in sensitivity of the tunnel current to changes in tip height and an increase in the effective tunneling area, as shown in Fig. 8(a), suggesting that both the vertical and lateral resolutions would decrease with increasing bias voltage.

The vertical resolution is calculated by $\Delta Z \approx \Delta I/(dI/dZ)$, where ΔI is the noise level of the current and dI/dZ is determined by the apparent barrier height. For our system, $\Delta I \sim 2$ pA at a constant current of 20 pA, and

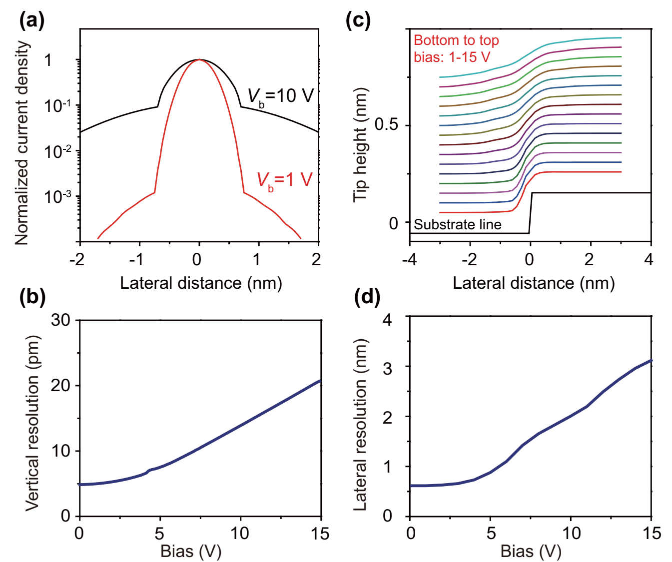

FIG. 8. (a) Calculated spatial distribution of the normalized tunneling current density at bias voltages of 1 and 10 V. (b) Simulated vertical resolution as a function of the bias voltage. (c) Simulated line scans across an atomic step at different bias voltages. (d) Simulated lateral resolution as a function of bias voltage as determined from the 10–90% variation of the line scans in (c).

the estimated vertical resolution as a function of bias voltage is shown in Fig. 8(b). To estimate the lateral resolution, we simulated the tip line scans at constant current across a monolayer step which was represented by a step function [Fig. 8(c)]. The line profile across the step becomes broader with increasing bias voltage, suggesting a decreasing lateral resolution with bias, as shown in Fig. 8(d).

F. Field emission and tunneling regimes

In order to extend the capacity of THz-STM to a wide range of bias voltages and minimize THz-induced surface modifications [48,49], it will be necessary to acquire the THz-induced tunnel current at low THz-pulse electric fields and correspondingly low THz-induced bias voltage. Although the THz-STM experiments in our work were limited to the field-emission regime due to the stability and the noise level of our system, our model can provide a guide towards realizing THz-STM on metals with lower THz-induced bias voltage. Firstly, the minimum detectable THz-induced current, $I_{THz,min}$, can be reduced by increasing the repetition rate of the THz pulses, minimizing preamp noise, or optimizing the stability of the STM system. Secondly, if tunneling stability is not compromised, the threshold THz electric field required to generate $I_{THz,min}$ can be lowered by reducing the tip-sample distance, thus extending the capacity of THz-STM to a wide range of bias voltages.

Figure 9 shows the calculated incident THz electric fields as a function of the relative tip heights needed to induce various tunnel currents, I_{THz}. To generate the minimum detectable I_{THz} of 2 e^-/pulse in the tunneling regime at, for example, $V_{THz,pk} = -3$ V in our system, a relative tip-height change of -0.35 nm was suggested by the simulations. However, the setpoint to reach this tip-sample distance would

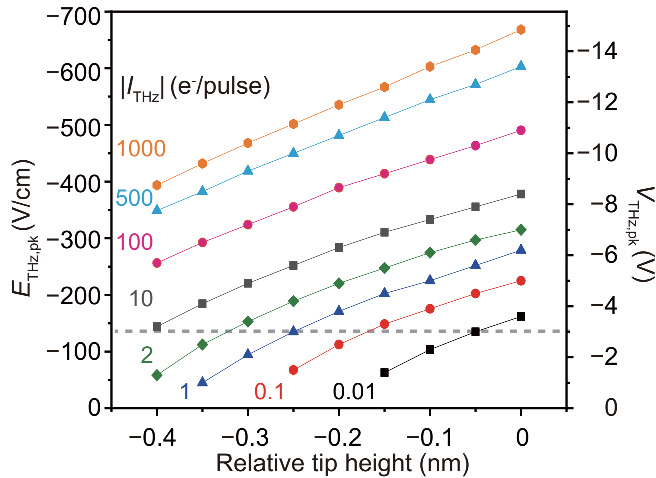

FIG. 9. Simulations of the incident THz electric field as a function of relative tip height at various THz-induced currents, I_{THz}, showing the required peak transient bias voltages and the tip-sample distance for different THz-STM signals. The original tip-sample distance was assumed to be 0.99 nm with $V_{\text{DC}} = 1$ V, $I_{\text{DC}} = 20$ pA. The gray dashed line indicates $V_{\text{THz,pk}} = -3.0$ V.

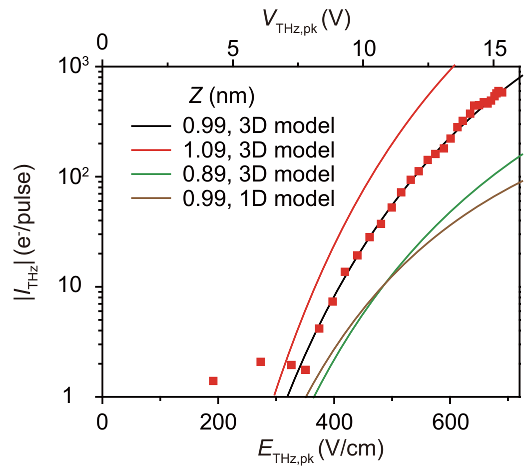

FIG. 10. Simulation of the measured THz-STM $I_{\text{THz}} - E_{\text{THz,pk}}$ curve (red dots) with different values for the initial tip-sample distance, Z. A comparison to a 1D tunneling model is also given. The tip-sample distance in all simulations is given by the setpoint of $V_{\text{DC}} = 1$ V and $I_{\text{DC}} = 20$ pA.

be $V_{\text{DC}} = 1$ V, $I_{\text{DC}} = 40$ nA or $V_{\text{DC}} = 0.1$ V, $I_{\text{DC}} = 4.7$ nA, which could not be achieved in our system due to instability associated with the open-flow cryostat. Another method is to reduce the lowest detectable $I_{\text{THz,min}}$ in the THz-STM system, which is determined by the minimum detectable average THz-induced current I_{min} via $I_{\text{THz,min}}[e^-/\text{pulse}] = I_{\text{min}}/(e \times f_{\text{rep}})$. This could be achieved by either increasing the repetition rate of the THz pulses from 250 kHz to 5 MHz or improving the stability of the THz-STM system. In a THz-STM system with a minimum detectable $I_{\text{THz,min}}$ of 0.1 e^-/pulse, a relative tip-height change of −0.2 nm would be required, corresponding to a setpoint of $V_{\text{DC}} = 1$ V, $I_{\text{DC}} = 1.5$ nA or $V_{\text{DC}} = 0.1$ V, $I_{\text{DC}} = 170$ pA.

V. CONCLUSIONS

In conclusion, we have measured the THz-induced tunnel currents and performed THz-STM imaging on a clean Cu(111) surface. Simulations based on an expanded steady-state tunneling model that considers the 3D geometry of the tip-sample interface successfully explain the observed THz current and nanoscale features at atomic step edges and defects in THz-STM images of the metal surface. Extreme THz pulse-induced current densities greater than 10^9A/cm^2 are observed, and the THz-induced bias voltage transient at the STM junction is quantified, which is critical for future energy-sensitive ultrafast THz-STM studies. TD-STM imaging of atomic steps and defects on a metal surface is also performed. Our work establishes an accurate framework for understanding and quantifying THz-induced currents and THz-STM imaging of metal surfaces, which will impact future experiments using THz-STM to explore ultrafast phenomena in materials on the nanoscale.

ACKNOWLEDGMENTS

This work was supported by the Natural Sciences and Engineering Research Council of Canada (NSERC), the Canada Foundation for Innovation (CFI), and the Alberta Innovates Technology Futures (AITF) Strategic Chairs Program. We are grateful for technical support from Greg Popowich, James Chaulk, and Beipei Shi.

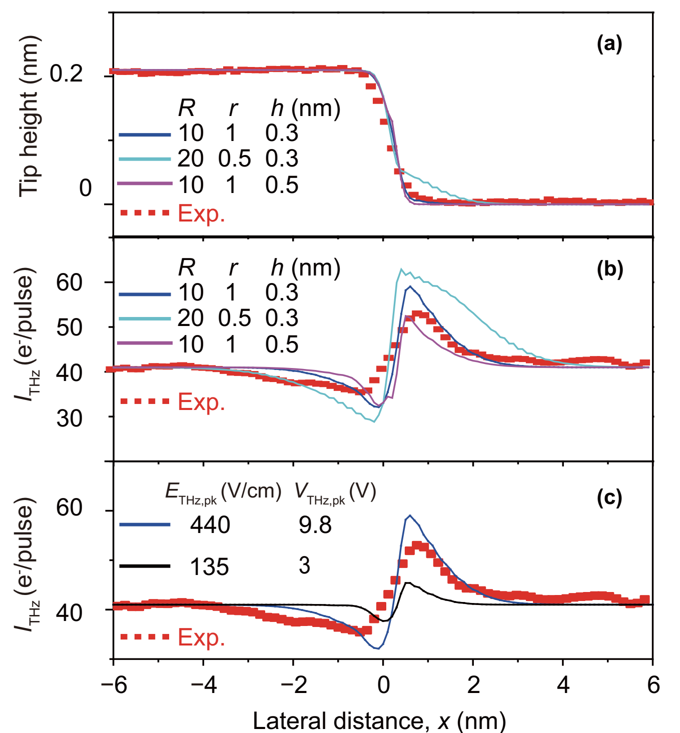

FIG. 11. (a) Effect of different parameters for the geometry of the tip on line-scan simulations for (a) the relative tip height and (b) THz-induced tunnel current across a monatomic step with. (c) Effect of incident THz electric field on line-scan simulation.

APPENDIX: DISCUSSION ON FIT PARAMETERS

The single-point simulation is sensitive to the distance, Z, between the tip and the sample, as shown in Fig. 10, where a change of 0.1 nm on the assumed tip-sample distance at the setpoint of 1 V and 20 pA would result in a dramatically different THz-induced current. A good fit from a 1D model would require a gap size of 1.2 nm, which is too large for a normal tunneling junction, and a different scale factor of 1/55 cm that would be inconsistent with the experimental data in Fig. 4. Thus, the size of gap is set to 0.99 nm at a setpoint of $V_{\mathrm{DC}} = 1$ V and $I_{\mathrm{DC}} = 20$ pA in all our simulations. The relative changes of the tip-sample distance with different bias voltages or different tunneling currents are determined by the experimental Z–V curves and I–Z curves.

In our simulations, the geometry of the tip was set by three parameters: the radii of the two spheres, R and r, and the distance h that the smaller sphere protrudes from the larger sphere [Fig. 2(c)]. As shown in Figs. 11(a) and 11(b), variations in the tip geometry parameters have a significant effect on how the simulations best fit the line profiles obtained in the observed STM and THz-STM images. The best-fit parameters for imaging are $R = 10$ nm, $r = 1$ nm, and $h = 0.3$ nm. As illustrated in Fig. 6, the effective tunneling area for THz-STM with a high transient bias voltage was much larger than that for steady-state STM with a low DC bias voltage, producing features in the THz-induced tunnel current images around the atomic step. This phenomenon would also exist with smaller THz-induced bias voltages in the tunneling regime, as shown for $V_{\mathrm{THz,pk}} = 3$ V in Fig. 11(c). Using only a single set of fit parameters for the tip geometry and a constant value for the near-field scaling factor for the THz-induced bias voltage, our 3D model provides a universal fit to the steady-state STM single-point measurements (Fig. 3), STM imaging line scans of atomic steps (Fig. 6), ultrafast THz-STM single-point measurements (Fig. 4), and ultrafast THz-STM imaging line scans of atomic steps (Fig. 6).

[1] Y. Terada, S. Yoshida, O. Takeuchi, and H. Shigekawa, Nat. Photonics **4**, 869 (2010).

[2] S. Loth, M. Etzkorn, C. P. Lutz, D. M. Eigler, and A. J. Heinrich, Science **329**, 1628 (2010).

[3] T. L. Cocker, V. Jelic, M. Gupta, S. J. Molesky, J. A. J. Burgess, G. De Los Reyes, L. V. Titova, Y. Y. Tsui, M. R. Freeman, and F. A. Hegmann, Nat. Photonics **7**, 620 (2013).

[4] M. Wagner, Z. Fei, A. S. McLeod, A. S. Rodin, W. Bao, E. G. Iwinski, Z. Zhao, M. Goldflam, M. Liu, and G. Dominguez, Nano Lett. **14**, 894 (2014).

[5] M. Eisele, T. L. Cocker, M. A. Huber, M. Plankl, L. Viti, D. Ercolani, L. Sorba, M. S. Vitiello, and R. Hober, Nat. Photonics **8**, 841 (2014).

[6] J. Jahng, J. Brocious, D. A. Fishman, S. Yampolsky, D. Nowak, F. Huang, V. A. Apkarian, H. K. Wickramasinghe, and E. O. Potma, Appl. Phys. Lett. **106**, 083113 (2015).

[7] V. Kravtsov, R. Ulbricht, J. M. Atkin, and M. B. Raschke, Nat. Nanotechnol. **11**, 459 (2016).

[8] T. L. Cocker, D. Peller, P. Yu, J. Repp, and R. Huber, Nature (London) **539**, 263 (2016).

[9] K. Yoshioka, I. Katayama, Y. Minami, M. Kitajima, S. Yoshida, H. Shigekawa, and J. Takeda, Nat. Photonics **10**, 762 (2016).

[10] V. Jelic, K. Iwaszczuk, P. H. Nguyen, C. Rathje, G. J. Hornig, H. M. Sharum, J. R. Hoffman, M. R. Freeman, and F. A. Hegmann, Nat. Phys. **13**, 591 (2017).

[11] P. Klarskov, H. Kim, V. L. Colvin, and D. M. Mittleman, ACS Photonics **4**, 2676 (2017).

[12] S. W. Li, S. Y. Chen, J. Li, R. Q. Wu, and W. Ho, Phys. Rev. Lett. **119**, 176002 (2017).

[13] A. Roslawska, P. Merino, C. Große, C. C. Leon, O. Gunnarsson, M. Etzkorn, K. Kuhnke, and K. Kern, Nano Lett. **18**, 4001 (2018).

[14] K. Yoshioka, I. Katayama, Y. Arashida, A. Ban, Y. Kawada, K. Konishi, H. Takahashi, and J. Takeda, Nano Lett. **18**, 5198 (2018).

[15] S. Yoshida, H. Hirori, T. Tachizaki, K. Yoshioka, Y. Arashida, Z. H. Wang, Y. Sanari, O. Takeuchi, Y. Kanemitsu, and H. Shigekawa, ACS Photonics **6**, 1356 (2019).

[16] M. Ludwig, G. Aguirregabiria, F. Ritzkowsky, T. Rybka, D. C. Marinica, J. Aizpurua, A. G. Borisov, A. Leitenstorfer, and D. Brida, Nat. Phys. **16**, 341 (2019).

[17] M. Garg and K. Kern, Science **367**, 411 (2020).

[18] M. Müller, N. Martín-Sabanés, T. Kampfrath, and M. Wolf, ACS Photonics **7**, 2046 (2020).

[19] F. Besenbacher, Rep. Prog. Phys. **59**, 1737 (1996).

[20] C. J. Chen, *Introduction to Scanning Tunneling Microscopy* (Oxford University Press, New York, 1993).

[21] R. Wiesendanger and W. Roland, *Scanning Probe Microscopy and Spectroscopy: Methods and Applications* (Cambridge University Press, London, 1994).

[22] M. Becker and R. Berndt, Phys. Rev. B **81**, 035426 (2010).

[23] J. M. Pitarke, F. Flores, and P. M. Echenique, Surf. Sci. **234**, 1 (1990).

[24] A. Samsavar, E. S. Hirschorn, T. Miller, F. M. Leibsle, J. A. Eades, and T. C. Chiang, Phys. Rev. Lett. **65**, 1607 (1990).

[25] M. F. Crommie, C. P. Lutz, and D. M. Eigler, Nature (London) **363**, 524 (1993).

[26] J. G. Simmons, J. Appl. Phys. **34**, 1793 (1963).

[27] G. Mesa, E. Dobado-Fuentes, and J. J. Saenz, J. Appl. Phys. **79**, 39 (1996).

[28] J. J. Saenz and R. Garcia, Appl. Phys. Lett. **65**, 3022 (1994).

[29] K. Torfason, A. Valfells, and A. Manolescu, Phys. Plasmas **23**, 123119 (2016).

[30] E. C. Teague, J. Res. Nat. Bur. Stand **91**, 171 (1986).

[31] P. Zhang, Sci. Rep. **5**, 9826 (2015).

[32] R. Paniago, R. Matzdorf, G. Meister, and A. Goldmann, Surf. Sci. **336**, 113 (1995).

[33] T. Ohwaki, H. Ishida, and A. Liebsch, Phys. Rev. B **68**, 155422 (2003).

[34] K. Wang, D. M. Mittleman, N. C. van der Valk, and P. C. Planken, Appl. Phys. Lett. **85**, 2715 (2004).

[35] L. Wimmer, G. Herink, D. R. Solli, S. V. Yalunin, K. E. Echternkamp, and C. Ropers, Nat. Phys. **10**, 432 (2014).

[36] T. T. Tsong, Phys. Rev. B **44**, 13703 (1991).

[37] C. Girard, C. Joachim, C. Chavy, and P. Sautet, Surf. Sci. **282**, 400 (1993).

[38] M. Olsen, M. Hummelgard, and H. Olin, PLOS One **7**, e30106 (2012).

[39] S. Kondo, S. Heike, M. Lutwyche, and Y. Wada, J. Appl. Phys. **78**, 155 (1995).

[40] R. H. Fowler and L. Nordheim, Proc. R. Soc. London, Ser. A **119**, 173 (1928).

[41] H. C. Miller, J. Franklin Inst. **282**, 382 (1966).

[42] V. T. Binh, N. Garcia, and S. T. Purcell, Adv. Imag. Elect. Phys. **95**, 63 (1996).

[43] G. N. Fursey and D. V. Glazanov, J. Vac. Sci. Technol. B **16**, 910 (1998).

[44] K. S. Yeong and J. T. L. Thong, J. Appl. Phys. **100**, 114325 (2006).

[45] G. Mesa and J. J. Sáenz, Appl. Phys. Lett. **69**, 1169 (1996).

[46] J. Wintterlin, J. Wiechers, H. Brune, T. Gritsch, H. Höfer, and R. J. Behm, Phys. Rev. Lett. **62**, 59 (1989).

[47] C. Wöll, S. Chiang, R. J. Wilson, and P. H. Lippel, Phys. Rev. B **39**, 7988 (1989).

[48] V. Jelic, Doctoral dissertation, University of Alberta, 2019.

[49] V. Jelic, D. Mildenberger, P. H. Nguyen, T. Wang, and F. A. Hegmann, CLEO: Science and Innovations, SW3D.1 (2018).